PHOTONICS Research

Anisotropic metamaterial-assisted all-silicon polarizer with 415-nm bandwidth

HONGNAN XU, DAOXIN DAI, AND YAOCHENG SHI*

Centre for Optical and Electromagnetic Research, State Key Laboratory for Modern Optical Instrumentation, Zhejiang University, Zijingang Campus, Hangzhou 310058, China
**Corresponding author: yaocheng@zju.edu.cn*

Received 27 August 2019; revised 12 October 2019; accepted 17 October 2019; posted 18 October 2019 (Doc. ID 376444); published 20 November 2019

Polarizers have been widely used in various optical systems to reduce polarization cross talk. The polarizers based on the silicon nanowire waveguide can provide chip-scale device size and a high polarization extinction ratio. However, the working bandwidth for the on-chip silicon polarizers is always limited (< ~100 nm) by the strong waveguide dispersion. In this paper, an on-chip all-silicon polarizer with an extremely broad working bandwidth is proposed and demonstrated. The device is based on a 180° sharp waveguide bend, assisted with anisotropic subwavelength grating (SWG) metamaterial cladding to enhance the polarization selectivity. For TE polarization, the effective refractive index for SWG is extraordinary, so the incident TE mode can propagate through the sharp waveguide bend. For TM polarization, the effective refractive index for SWG is ordinary, so the incident TM mode will be coupled into the radiation mode regardless of the wavelength. The fabricated polarizer shows low loss (<1 dB) and high polarization extinction ratio (>20 dB) over a >415 nm bandwidth from 1.26 to 1.675 μm, which is at least fourfold better than what has been demonstrated in all previous works. To the best of our knowledge, such a device is the first all-silicon polarizer that covers O-, E-, S-, C-, L-, and U-bands.

https://doi.org/10.1364/PRJ.7.001432

1. INTRODUCTION

The polarizer is a basic component utilized in various optical systems, e.g., biological imaging, optical gyroscope, and optical communication systems [1,2] to filter out undesired polarization and reduce polarization cross talk. The polarizers based on the birefringent fibers [3,4], multilayer thin films [5,6], and wire grids [7,8] have been demonstrated, but all suffer from the bulky device size. Photonic integrated circuits (PICs) based on silicon-on-insulators (SOIs) have been widely used to develop various on-chip nanophotonic devices with ultrasmall footprints [9], taking advantages of the compatibility with the complementary metal oxide semiconductor (CMOS) fabrication process and subwavelength light confinement of the silicon nanowire waveguide. Various on-chip silicon polarizers have been reported over recent years. One commonly used scheme is based on the highly birefringent waveguide with strong polarization-dependent loss (PDL), e.g., shallowly etched waveguide [10] or adiabatic waveguide bend [11]. However, this type of polarizer always suffers from a relatively large footprint, since the PDL is limited in the silicon nanowire waveguide, even with extreme structural dimensions. The silicon hybrid plasmonic/graphene structures have been introduced to enhance the PDL and reduce the device size [12–15]. The major disadvantage for silicon hybrid plasmonic polarizers is the significant excess loss (EL ≈ 1–3 dB) due to the intrinsic ohmic loss in the metal [12,13]. The ELs for graphene-based polarizers are much lower (EL < 1 dB) [14,15], but such structures are usually difficult to fabricate due to the CMOS-incompatible fabrication process. Asymmetric directional couplers (ADCs) can also be utilized as polarizers [16,17]. For ADC-based polarizers, phase-matched polarization can be coupled into the adjacent waveguide and diffracted into free space, while phase-mismatched polarization can propagate through with low loss. Such polarizers have been employed to improve the performance of polarization beam splitters (PBSs) and polarization rotators (PRs) [18–22]. However, ADCs are usually wavelength-sensitive, leading to a relatively narrow working bandwidth (BW ≈ 80 nm). The polarization selection can also be realized by using Bragg gratings [23–28]. The idea is to optimize the structural parameters so that only one polarization can be supported by the Bloch mode, while the orthogonal polarization will be rejected. Such polarizers can provide high polarization extinction ratios (PER > 30 dB) and low ELs (EL < 1 dB). However, for all these Bragg-grating-based structures, the undesired polarization is reflected, so that such polarizers cannot be cascaded directly after the light source, and an

additional isolator or circulator is required. Furthermore, in all previous works, only a restricted working bandwidth (BW $<$ ~100 nm) can be experimentally realized, due to the strong dispersion in the silicon nanowire waveguide, which limits its applications, especially in the high-capacity optical communication systems [29–33]. Recently, a silicon hybrid plasmonic polarizer with an ultrabroad working bandwidth was theoretically demonstrated, where the subwavelength metal nanostripes are exploited to diffract the undesired polarization [34]. However, such subwavelength metal nanostripes also introduce quite large EL (EL ≈ 1.7 dB), and there is no experimental demonstration for such a structure. In general, it is still a challenge to realize the on-chip all-silicon polarizer with compact device size, low EL, high PER, and especially broad working bandwidth.

The subwavelength grating (SWG) is a kind of anisotropic metamaterial (AM) formed by a series of dielectric nanostripes with deep subwavelength scale [35–38]. The SWG metamaterial shows great potential in dispersion engineering, index mapping, and anisotropy controlling, leading to a wide utility in PICs, such as fiber-chip coupling [39–41], power splitting [42–44], mode manipulation [45–48], and polarization handling [49–54]. In Ref. [55], the SWG metamaterial is employed to control the evanescent wave of the silicon nanowire waveguide in a single TE polarization to enhance the integration density. In Ref. [56], the SWG metamaterial has been utilized to realize a polarizer; however, the device size for such a structure is quite large (≈60 μm), and the working bandwidth is still restricted (BW ≈ 100 nm). In this paper, we propose and demonstrate an on-chip all-silicon polarizer based on a 180° sharp waveguide bend assisted with anisotropic SWG metamaterial cladding. The polarization selectivity can be significantly enhanced by the anisotropic SWG metamaterial. For TE polarization, the SWG effective refractive index is extraordinary, leading to a confined mode with low bending loss, while for TM polarization, the SWG effective refractive index is ordinary, leading to a leaky mode with significant bending loss. In this way, only TE-polarized light can propagate through the metamaterial-assisted waveguide bend, while the TM-polarized light will be efficiently filtered out. Moreover, such polarization-dependent bending loss (PDBL) can be strong enough regardless of the wavelength, leading to an extremely broad working bandwidth. Experimental results show that such a metamaterial-assisted polarizer can provide low EL (EL $<$ 1 dB) and high PER (PER $>$ 20 dB) from over 1.26 to 1.675 μm (BW $>$ 415 nm), which is at least fourfold better than found in all previous works. To the best of our knowledge, such a device is the first all-silicon polarizer that can cover O-, E-, S-, C-, L-, and U-bands.

2. DESIGN AND ANALYSIS

Figure 1(a) shows the configuration of the proposed polarizer, which is based on a 180° sharp waveguide bend assisted with anisotropic SWG metamaterial cladding. In this paper, the device is designed based on the SOI platform with a 250-nm silicon top layer ($n_{Si} \approx 3.46$) and a 3-μm oxide buffer layer ($n_{SiO2} \approx 1.45$). The upper cladding is chosen to be air ($n_{air} \approx 1$). In the SWG metamaterial, the nanostripes are

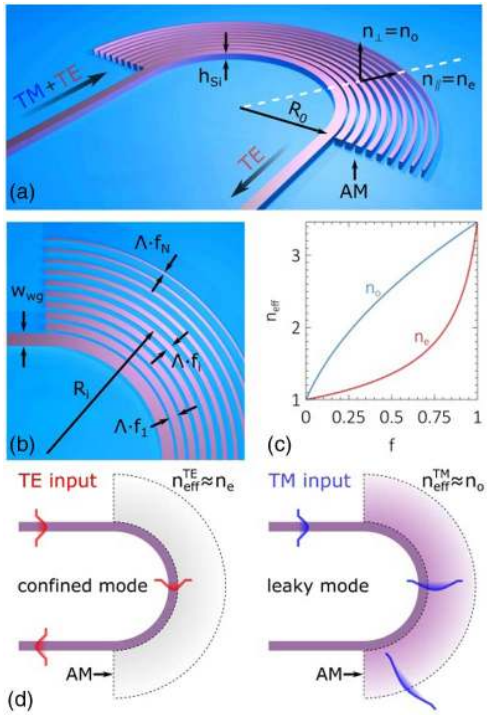

Fig. 1. (a) 3D view of the proposed on-chip all-silicon polarizer utilizing the AM with some key parameters labeled. The white dashed line shows the optical axis orientation of the SWG metamaterial. (b) The enlarged top view of the input section with some key parameters labeled; (c) calculated extraordinary (n_e) and ordinary (n_o) effective refractive indices for the SWG metamaterial with varied duty cycle f; (d) working principle for the metamaterial-assisted polarizer. For TE polarization, the SWG effective refractive index is extraordinary ($n_{\text{eff}}^{\text{TM}} \approx n_\parallel = n_e$), which is much smaller than the silicon refractive index, leading to the confined mode and negligible bending loss, so the incident TE mode will propagate through the sharp bend. For TM polarization, the SWG effective refractive index is ordinary ($n_{\text{eff}}^{\text{TM}} \approx n_\perp = n_o$), which is close to the silicon refractive index, leading to the leaky mode and strong bending loss, so the incident TM mode will be coupled into the radiation mode.

parallel to the bending direction, and the optical axis is perpendicular to the tangent direction [see Figs. 1(a) and 1(b)]. Thus, the bending radius for the nanostripe can be written as

$$R_i = R_0 + w_{\text{wg}}/2 + \Lambda \cdot (i - 1/2), \tag{1}$$

where R_i is the bending radius for the ith nanostripe, R_0 is the bending radius for the sharp waveguide bend, w_{wg} is the waveguide width, and Λ is the pitch for the SWG metamaterial [see Fig. 1(b)]. The effective refractive index tensor for the SWG metamaterial can be obtained by using Rytov's formulas [57],

$$\boldsymbol{n}_{\text{eff}} = \text{diag}[n_\parallel, n_\perp] = \text{diag}[n_e, n_o], \tag{2}$$

$$1/n_e^2 = f/n_{\text{Si}}^2 + (1 - f)/n_{\text{air}}^2, \tag{3}$$

$$n_o^2 = f \cdot n_{\text{Si}}^2 + (1 - f) \cdot n_{\text{air}}^2, \tag{4}$$

where $n_{\|}/n_{\perp}$ is the effective refractive index for the light with electric component parallel/perpendicular to the optical axis, n_e/n_o is the extraordinary/ordinary refractive index [see Fig. 1(a)], and f is the SWG duty cycle [see Fig. 1(b)]. Figure 1(c) shows the calculated n_e and n_o with SWG duty cycle varying from $f = 0$ to $f = 1$ using Eqs. (3) and (4). From Fig. 1(c), one can find that the ordinary refractive index is always higher than the extraordinary refractive index ($n_o > n_e$), e.g., the effective refractive indices are calculated to be $n_o = 3.04$ and $n_e = 1.79$ when $f = 0.75$. For TE polarization with a major electric component parallel to the optical axis, the effective refractive index is nearly extraordinary ($n_{\text{eff}}^{\text{TM}} \approx n_{\|} = n_e$), which is much smaller than the silicon refractive index. Thus, the TE mode can be well confined in the silicon core region and propagate through the sharp waveguide bend with low bending loss, as shown in Fig. 1(d). On the other hand, for TM polarization with a major electric component perpendicular to the optical axis, the effective refractive index is nearly ordinary ($n_{\text{eff}}^{\text{TM}} \approx n_{\perp} = n_o$), which is quite close to the silicon refractive index, leading to the leaky mode and significant bending loss. Thus, the incident TM mode will be coupled into the radiation mode in the SWG cladding region, as shown in Fig. 1(d). Furthermore, the SWG duty cycle decreases with the radius, so that the radiation mode in the SWG cladding region can be adiabatically diffracted into free space. Such a polarizer should be wavelength-insensitive, since the PDBL can be strong enough regardless of the wavelength if the bending radius and SWG duty cycle are properly chosen.

The SWG duty cycle is designed to satisfy the following equation:

$$f_i = f_M + (f_m - f_M) \cdot (i - 1)/(N - 1), \tag{5}$$

where f_i is the SWG duty cycle for the ith nanostripe, f_M/f_m is the maximum/minimum SWG duty cycle, and N is the number of the SWG periods [see Fig. 1(b)]. The waveguide width is chosen to be $w_{\text{wg}} = 360$ nm to satisfy the single-mode condition over all the optical communication bands. The SWG pitch is chosen to be $\Lambda = 300$ nm to meet the subwavelength requirement. The minimum SWG duty cycle is chosen to be $f_m = 0.2$ to ensure an achievable minimum feature size of $\Lambda \cdot f_m = 60$ nm. Here, the number of the SWG periods is chosen to be $N = 10$ as an initial setting. We calculate the TE and TM mode transmittance spectra for the metamaterial-assisted polarizer with varied f_M and R_0 based on the three dimensional finite-difference time-domain (3D FDTD) method using Lumerical commercial software, as shown in Fig. 2. The mesh grid size is chosen as $dx = dy = dz = 10$ nm to satisfy the simulation accuracy requirement for the subwavelength structures. The eigenmode expansion (EME) method is utilized at the output port to filter out the scattering field and obtain the TE and TM mode transmittances. From the results, the TE mode transmittance is much higher than that of the TM mode transmittance, indicating a significant PDBL. Moreover, the TE and TM mode transmittances can be $T_{\text{TE}} > -1$ dB and $T_{\text{TM}} < -20$ dB over all the optical communication bands (1.26–1.675 μm wavelength) when the waveguide bending radius and maximum SWG duty cycle are chosen as $R_0 = 3.5$ μm and $f_M = 0.75$ (see the dashed lines in Fig. 2).

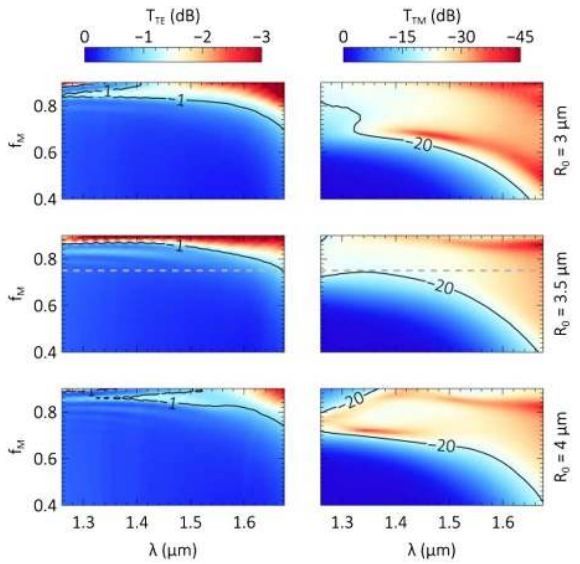

Fig. 2. Calculated transmittance spectra for TE and TM modes with varied maximum SWG duty cycle (f_M) and bending radius (R_0).

We calculate the EL spectra for the metamaterial-assisted polarizer with different SWG period number varying from $N = 7$ to $N = 12$ using the 3D FDTD method, as shown in Fig. 3(a). Here, the bending radius and maximum SWG duty cycle are set to be $R_0 = 3$ μm and $f_M = 0.75$, as analyzed above. The EL is defined as

$$\text{EL} = -10 \log_{10}(T_{\text{TE}}), \tag{6}$$

where T_{TE} is the transmittance when the TE mode is launched. One could find that the EL is always EL < ~1 dB over the whole bandwidth, and such a broadband property is nearly

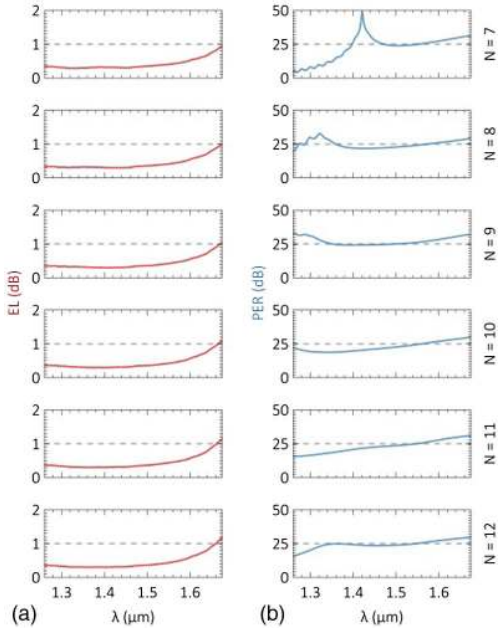

Fig. 3. Calculated (a) EL and (b) PER spectra with varied SWG period number (N).

independent of the SWG period number N, since the TE mode is well confined and the interaction with the SWG cladding is quite weak. We then calculate the PER spectra for the metamaterial-assisted polarizer with varied SWG period N using the 3D FDTD method, as shown in Fig. 3(b). The PER is defined as

$$\mathrm{PER} = 10\log_{10}(T_{\mathrm{TE}}/T_{\mathrm{TM}}), \tag{7}$$

where $T_{\mathrm{TE}}/T_{\mathrm{TM}}$ is the transmittance when the TE/TM mode is launched. From the spectra, the PER can be PER < 10 dB around the O-band when the SWG period number is $N = 7$. One can also find a sharp peak in the spectrum at ~1.42 μm wavelength with $N = 7$. Such a phenomenon is primarily induced by the TM mode interference (see Appendix A). The incident TM mode can be coupled into the radiation mode by the SWG metamaterial. However, if the SWG period number is not large enough (e.g., $N = 7$), the excited TM radiation mode will not be completely diffracted into free space. Some part of the TM mode remains in the SWG cladding region and excites the "cladding mode" [58], which might interfere with the leaky mode in the silicon waveguide and reduce the PER, especially at the shorter wavelengths (light confinement is stronger). To improve the PER at the shorter wavelengths, one could choose a relatively large SWG period number N to satisfy the adiabatic condition. However, one might find that the TM mode interference still exists even if the SWG period number N is quite large (see Appendix A), since the minimum SWG duty cycle is chosen to be $f_m = 0.2$, with a corresponding effective refractive index of $n_{\mathrm{eff}}^{\mathrm{TM}} \approx 1.79$ and a refractive index mismatch of $n_{\mathrm{eff}}^{\mathrm{TM}} - n_{\mathrm{air}} = 0.79$, which leads to an incomplete diffraction for TM polarization. Such TM mode interference can be inhibited further by using an even smaller $f_m = 0.02$ to reduce the refractive index mismatch (see Appendix A). However, it is difficult to fabricate the SWG metamaterial with such a small duty cycle. To overcome this obstacle, one could obtain a destructive interference at the output port to reduce the TM mode transmittance by carefully choosing the SWG period number N. From Fig. 3(b), the PER can be PER > 25 dB over the 1.26–1.675 μm wavelength range when the SWG period number is chosen to be $N = 9$.

The optimized parameters for the metamaterial-assisted polarizer are summarized as: $h_{\mathrm{Si}} = 250$ nm, $w_{\mathrm{wg}} = 360$ nm, $R_0 = 3.5$ μm, $\Lambda = 300$ nm, $f_M = 0.75$, $f_m = 0.2$, and $N = 9$. We calculate the light propagation profiles and transmittance spectra for the optimized polarizer when TE and TM modes are incident, as shown in Figs. 4(a) and 4(b). From the profiles shown in Fig. 4(a), the incident TE mode can propagate directly through the waveguide bend with low loss, while the incident TM mode can be efficiently coupled into the radiation mode with negligible power remaining in the silicon waveguide. Moreover, such polarization-selective propagation can be observed at different wavelengths ($\lambda = 1.26$, 1.55, 1.675 μm), as shown in Fig. 4(a). From the spectra shown in Fig. 4(b), the EL and PER are calculated to be EL ≈ 0.4 dB and PER ≈ 26 dB at the 1.55 μm wavelength. The low EL < 1 dB and high PER > 25 dB can be observed over a BW = 415 nm bandwidth from 1.26 to 1.675 μm. Further simulations also show that the reflection for the

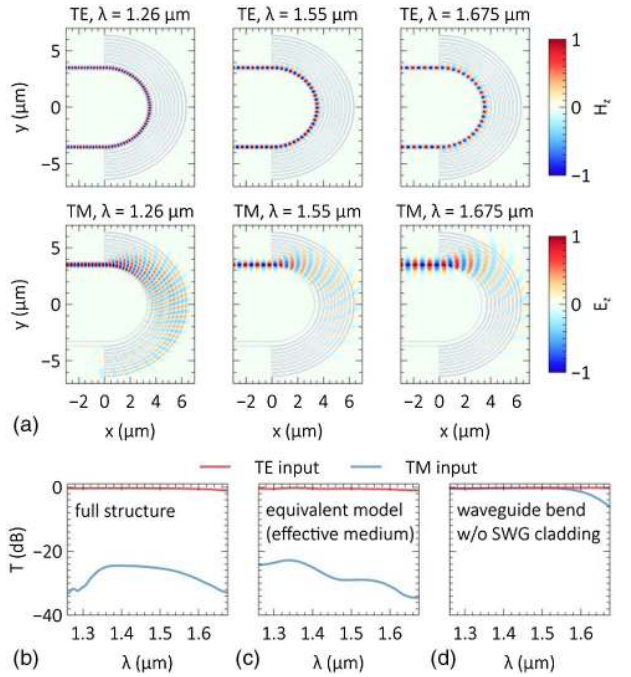

Fig. 4. (a) Calculated TE and TM light propagation profiles for the optimized polarizer at three different wavelengths ($\lambda = 1.26$, 1.55, 1.675 μm). The calculated transmittance spectra for the (b) optimized polarizer with full structure, (c) optimized polarizer with effective medium equivalence, and (d) waveguide bend without SWG cladding.

optimized polarizer can be negligible (< −20 dB) for both TE and TM modes, so that the proposed metamaterial-assisted polarizer can be directly cascaded after the light source without an additional isolator or circulator. We also calculate the transmittance spectra for the polarizer with SWG cladding replaced by the effective medium using Eqs. (3) and (4), as shown in Fig. 4(c), which shows great agreement with the calculation results for the full structure without any equivalence [see Fig. 4(b)], indicating that the equivalent model is quite accurate. As a comparison, we also calculate the transmittance spectra for the sharp waveguide bend without the SWG cladding, as shown in Fig. 4(d). It can be found from the spectra that the transmittances are almost the same over the 1.26–1.55 μm wavelength range between TE and TM polarizations, and the maximum PER is only PER < 6 dB at 1.675 μm wavelength, indicating the strong anisotropy enhancement of the SWG metamaterial. We also investigate the fabrication tolerance of the proposed metamaterial-assisted polarizer, as shown in Fig. 5. The major fabrication errors include the deviations of the waveguide height δh_{Si}, the waveguide width δw_{wg}, the maximum SWG nanostripe width $\Lambda \cdot \delta f_M$, and the minimum SWG nanostripe width $\Lambda \cdot \delta f_m$. It can be found that the low EL < 1 dB, high PER > 20 dB, and broad bandwidth BW > 415 nm can still be maintained even if the parameters are deviated over a ±10 nm range. Further Monte Carlo simulations show that the low EL < 1.5 dB and high PER > 15 dB can still be obtained with arbitrary multiparameter deviations over a ±10 nm range, leading to an easy fabrication process [59].

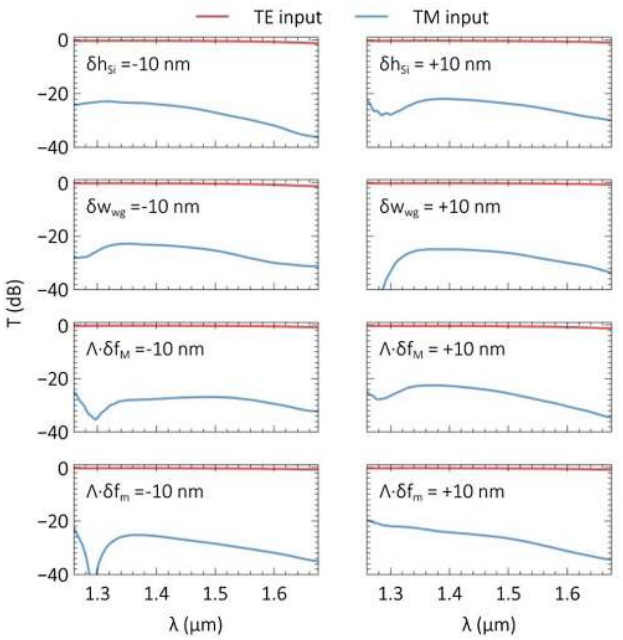

Fig. 5. Calculated transmittance spectra for the metamaterial-assisted polarizer with deviated parameters.

3. FABRICATION AND CHARACTERIZATION

The proposed metamaterial-assisted polarizer was fabricated on the SOI platform with a 250-nm Si top layer and a 3-μm SiO_2 buffer layer. An electron beam lithography (EBL, Raith 150 II) process was carried out to define the pattern with the MA-N 2401 photoresist. The silicon top layer was then fully etched using an inductively coupled plasma (ICP) etching process. Another overlay exposure with the PMMA photoresist followed by a 70-nm shallow etching process was performed to fabricate grating couplers (GCs) at each input and output port for chip-fiber coupling and polarization selectivity [60]. All the input and output ports are separated by a >500 μm distance. However, it is quite difficult to measure the transmittance spectra over the 1.26–1.675 μm wavelength range with a single measurement, due to the limited working bandwidth for the GC. The measurement bandwidth can be expanded to ~200 nm by adjusting the fiber probe tilt angle from $\theta_{\text{fiber}} = 10°$ to $\theta_{\text{fiber}} = 30°$ (see Appendix B), but it still cannot cover the 415-nm wavelength span required for the measurement. To overcome this obstacle, four sets of devices with the same polarizers but different GCs were fabricated closely on the same chip, as shown in Fig. 6(a). Figure 6(b) shows the scanning electron microscopy (SEM) image of the fabricated polarizer. The input ports [I1, I2] and output ports [O1, O2] were connected with TE-type GCs, while the input ports [I3, I4] and output ports [O3, O4] were connected with TM-type GCs. The TE-type GCs at [I1, O1]/[I2, O2] ports were designed to cover the [O, E]/[S, C, L, U] bands. The TM-type GCs at [I3, O3]/[I4, O4] ports were designed to cover the [O, E]/[S, C, L, U] bands. The straight single-mode waveguides were also fabricated on the same chip for normalization. The optimized parameters for the GCs are summarized in Appendix B, Table 2. The working polarization and

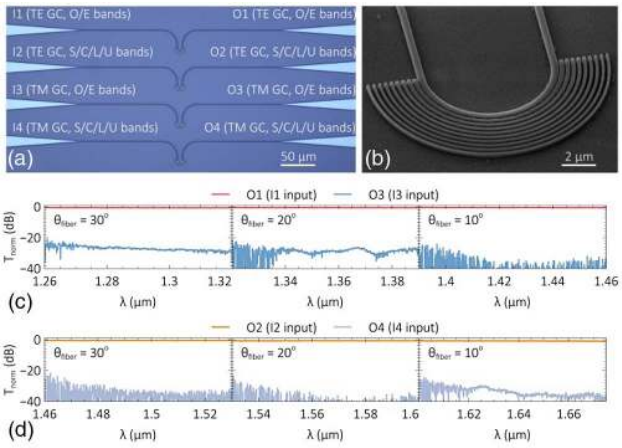

Fig. 6. (a) Microscope image of the fabricated devices; (b) SEM image of the fabricated metamaterial-assisted polarizer. The measured transmittance spectra over (c) O-, E-bands and (d) S-, C-, L-, U-bands.

measurement wavelength range at each input and output port are labeled in Fig. 6(a). For example, to obtain the TE transmittance over [O, E] bands, one could choose the I1 input port and the O1 output port, and set the fiber probe tilt angle as $\theta_{\text{fiber}} = 10°/20°/30°$ to measure the transmittance spectra over 1.26–1.32 μm/1.32–1.39 μm/1.39–1.46 μm wavelength ranges. In this way, one could characterize the transmission responses for different polarizations and wavelength ranges by choosing different input and output ports with different fiber probe tilt angles. A supercontinuum source and an optical spectrum analyzer were utilized to measure the transmission responses for the fabricated devices. Figures 6(c) and 6(d) show the measured transmittance spectra. The ELs of the GCs have been deducted to normalize the transmittance spectra (see Appendix B). A high PER of PER > 20 dB can be observed from the spectra over the 1.26–1.675 μm wavelength

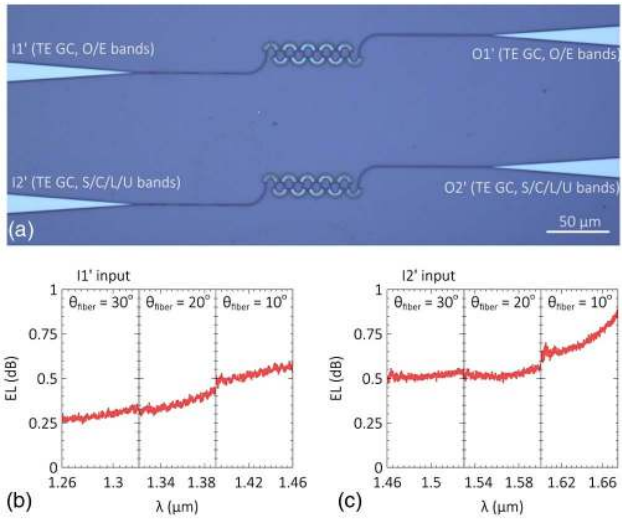

Fig. 7. (a) Microscope image of the cascaded polarizers. The measured single polarizer EL spectra over (b) O-, E-bands and (c) S-, C-, L-, U-bands.

range, which agrees well with the simulation results. However, it is difficult to accurately characterize the ELs due to the measurement noises. We fabricated some testing structures with 10 identical polarizers cascaded in a series to decrease the measurement noise and evaluate the low ELs accurately, as shown in Fig. 7(a). The input port I1′/I2′ and output port O1′/O2′ were connected with TE-type GCs covering [O, E]/[S, C, L, U] bands. Figures 7(b) and 7(c) show the measured EL spectra for a single polarizer. The EL was measured to be EL ≈ 0.5 dB at the central wavelength of 1.55 μm. Low ELs of EL < 1 dB can be observed over the 415-nm bandwidth from 1.26 to 1.675 μm.

4. CONCLUSION

In conclusion, we have proposed and demonstrated a metamaterial-assisted on-chip all-silicon polarizer with an extremely broad working bandwidth. The device is based on a 180° sharp waveguide bend, assisted with anisotropic SWG metamaterial cladding. For TE polarization, the SWG effective refractive index is extraordinary, which is much smaller than the silicon refractive index, leading to the strong light confinement and negligible bending loss. For TM polarization, the SWG effective refractive index is ordinary, which is quite close to the silicon refractive index, leading to weak light confinement and significant bending loss. Thus, only TE-polarized light can propagate through the metamaterial-assisted waveguide bend, while TM-polarized light will be efficiently filtered out. Such a device is designed based on the all-silicon platform without metal or graphene. The footprint of the present metamaterial-assisted polarizer is as small as ∼13 μm × 6.5 μm. The measurement shows low EL (EL < 1 dB) and high PER (PER > 20 dB) over O-, E-, S-, C-, L-, and U-bands from 1.26 to 1.675 μm. We have compared the performances of several reported on-chip silicon polarizers in Table 1 (only experimental results). It can be found that the working bandwidth is limited, as BW ≈ 100 nm for all the previous works, while this metamaterial-assisted polarizer could provide an ultrabroad bandwidth BW > 415 nm, which is at least fourfold better. To the best of our knowledge, the present structure is the first experimental demonstration of an on-chip all-silicon polarizer that covers O-, E-, S-, C-, L-, and U-bands. We believe such a device could find applications, especially in high-performance large-capacity optical communication systems.

Table 1. Performance Comparison of Several On-Chip Silicon Polarizers

Structures	Platform	Size (μm)	EL (dB)	PER (dB)	BW (nm)
[10]	SOI	1000	<5	25	100
[11]	SOI	63 × 9.5	<0.37	>27.6	100
[13]	SOI + Cr	30	2–3	>23	60
[17]	SOI	≈30	≈1	>15	>80
[23]	SOI	≈9	<1	>20	∼60
[24]	SOI	≈4	≈1	>30	>50
[26]	SOI + Au	≈6	2.8–4.9	>24	60
[56]	SOI	60	≈0.4	≈30	>100
This work	SOI	13 × 6.5	<1	>20	>415

APPENDIX A: TM MODE INTERFERENCE ANALYSIS

The TM-polarized light in the silicon core region can be coupled into the SWG cladding region when propagating in the sharp waveguide bend, which is then diffracted into free space by the index-gradient SWG metamaterial. The "cladding mode" [58] could be excited if the diffraction process is incomplete, which can lead to TM mode interference and reduce the PER. The TM mode should be completely diffracted when the SWG period number N is large enough and the adiabatic condition is satisfied. We calculate TM transmittance spectra with $f_m = 0.2$, $f_M = 0.75$, and SWG period number varying from $N = 5$ to $N = 25$, as shown in Fig. 8(a). From the spectra, the interference fringe still exists around the O-band even if the SWG period number is quite large ($N = 25$), which is due to the relatively large minimum SWG duty cycle ($f_m = 0.2$). Such an interference fringe is related to the peak in the PER spectra (see Fig. 3). To inhibit the TM mode interference and enhance the PER, one could choose an even smaller f_m to reduce the refractive index mismatch and ensure a complete diffraction process. Figure 8(b) shows the calculated TM transmittance spectra with $f_m = 0.02$, $f_M = 0.75$, and SWG period number varying from $N = 5$ to $N = 25$. One can find that the TM mode interference is quite weak with $f_m = 0.02$, indicating complete diffraction. However, it is difficult to fabricate the SWG metamaterial with such a small duty cycle ($f_m = 0.02$). To overcome this obstacle, the minimum duty cycle is still chosen to be $f_m = 0.2$ to ensure an achievable fabrication process. The SWG period number is then chosen to be $N = 9$ to obtain a destructive interference and reduce the TM mode output.

APPENDIX B: DESIGN AND MEASUREMENT OF GCS

The GCs are utilized at each input and output port for device characterization. The measurement bandwidth can be

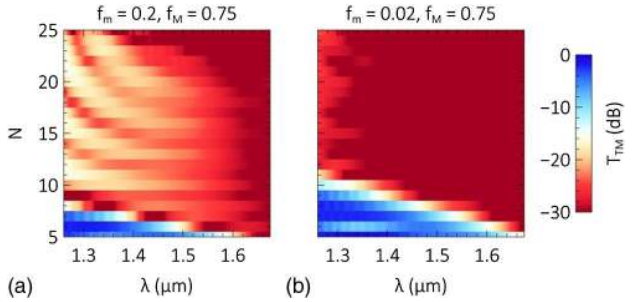

Fig. 8. Calculated TM mode transmittance spectra with varied SWG period number (N) and minimum SWG duty cycle (f_m).

Table 2. Optimized Parameters of Four Different GCs

Pol.	Wavelength Range (μm)	Λ_{grt} (nm)	f_{grt}	h_{etch} (nm)
TE	1.26–1.46 (O-, E-bands)	520	0.6	70
TE	1.46–1.675 (S-, C-, L-, U-bands)	650	0.5	70
TM	1.26–1.46 (O-, E-bands)	700	0.75	70
TM	1.46–1.675 (S-, C-, L-, U-bands)	980	0.75	70

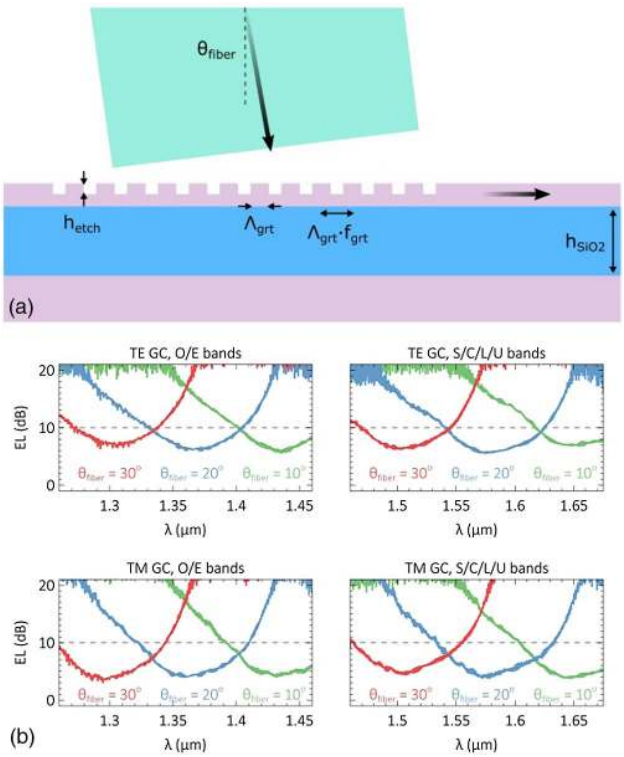

Fig. 9. (a) Configuration of the GC with some key parameters labeled; (b) measured EL spectra for the fabricated GCs with different fiber probe tilt angles θ_{fiber}.

expanded to >200 nm by adjusting the fiber probe tilt angle from $\theta_{\text{fiber}} = 10°$ to $\theta_{\text{fiber}} = 30°$ [51], but it still cannot cover the required measurement wavelength range (1.26–1.675 μm). Four different GCs with different parameters are utilized to overcome this obstacle.

The GCs are designed for different polarizations and working wavelengths based on the 250-nm SOI platform with an $h_{\text{SiO2}} = 3$ μm buffer layer. The working polarization, measurement wavelength range, and optimized parameters of these GCs are summarized in Table 2. Figure 9 shows the measured EL spectra for the four different GCs with varied θ_{fiber}. From the spectra, the GCs could cover the 1.26–1.675 μm wavelength range with low EL < ~10 dB. In this way, one could obtain the TE and TM mode transmittances over all the optical communication bands by choosing different GCs and different fiber probe tilt angles.

Funding. National Major Research and Development Program (2018YFB2200200); National Natural Science Foundation of China (11861121002, 61922070).

REFERENCES

1. D. Dai, J. Bauters, and J. E. Bowers, "Passive technologies for future large-scale photonic integrated circuits on silicon: polarization handling, light non-reciprocity and loss reduction," Light Sci. Appl. **1**, e1 (2012).
2. D. Dai, L. Liu, S. Gao, D. X. Xu, and S. He, "Polarization management for silicon photonic integrated circuits," Laser Photon. Rev. **7**, 303–328 (2013).
3. T. Hosaka, K. Okamoto, and T. Edahiro, "Fabrication of single-mode fiber-type polarizer," Opt. Lett. **8**, 124–126 (1983).
4. R. A. Bergh, H. C. Lefevre, and H. J. Shaw, "Single-mode fiber-optic polarizer," Opt. Lett. **5**, 479–481 (1980).
5. J. C. Monga, P. D. Gupta, and D. D. Bhawalkar, "Design of multi-wavelength thin-film polarizers for high-power laser systems," Appl. Opt. **23**, 3538–3540 (1984).
6. M. Gilo and K. Rabinovitch, "Design parameters of thin-film cubic-type polarizers for high power lasers," Appl. Opt. **26**, 2518–2521 (1987).
7. J. Wang, Y. Zhao, I. Agha, and A. M. Sarangan, "SU-8 nanoimprint fabrication of wire-grid polarizers using deep-UV interference lithography," Opt. Lett. **40**, 4396–4399 (2015).
8. J. Wang, W. Zhang, X. Deng, J. Deng, F. Liu, P. Sciortino, and L. Chen, "High-performance nanowire-grid polarizers," Opt. Lett. **30**, 195–197 (2005).
9. W. Bogaerts and L. Chrostowski, "Silicon photonics circuit design: methods, tools and challenges," Laser Photon. Rev. **12**, 1700237 (2018).
10. D. Dai, Z. Wang, N. Julian, and J. E. Bowers, "Compact broadband polarizer based on shallowly-etched silicon-on-insulator ridge optical waveguides," Opt. Express **18**, 27404–27415 (2010).
11. H. Zafar, P. Moreira, A. M. Taha, B. Paredes, M. S. Dahlem, and A. Khilo, "Compact silicon TE-pass polarizer using adiabatically-bent fully-etched waveguides," Opt. Express **26**, 31850–31860 (2018).
12. M. Z. Alam, S. J. Aitchison, and M. Mojahedi, "Compact and silicon-on-insulator-compatible hybrid plasmonic TE-pass polarizer," Opt. Lett. **37**, 55–57 (2011).
13. X. Sun, M. Z. Alam, S. J. Wagner, J. S. Aitchison, and M. Mojahedi, "Experimental demonstration of a hybrid plasmonic transverse electric pass polarizer for a silicon-on-insulator platform," Opt. Lett. **37**, 4814–4816 (2012).
14. X. Yin, X. Ke, L. Chen, T. Zhang, J. Li, Z. Zhu, and X. Li, "Ultra-broadband TE-pass polarizer using a cascade of multiple few-layer graphene embedded silicon waveguides," J. Lightwave Technol. **34**, 3181–3187 (2015).
15. X. Yin, T. Zhang, L. Chen, and X. Li, "Ultra-compact TE-pass polarizer with graphene multilayer embedded in a silicon slot waveguide," Opt. Lett. **40**, 1733–1736 (2015).
16. B. Ni and J. Xiao, "A compact silicon-based TE-pass polarizer using three-guide directional couplers," IEEE Photon. Technol. Lett. **29**, 1631–1634 (2017).
17. H. Xu and Y. Shi, "On-chip silicon TE-pass polarizer based on asymmetrical directional couplers," IEEE Photon. Technol. Lett. **29**, 861–864 (2017).
18. H. Xu and Y. Shi, "Ultra-compact and highly efficient polarization rotator utilizing multi-mode waveguides," Opt. Lett. **42**, 771–774 (2017).
19. J. Wang, D. Liang, Y. Tang, D. Dai, and J. E. Bowers, "Realization of an ultra-short silicon polarization beam splitter with an asymmetrical bent directional coupler," Opt. Lett. **38**, 4–6 (2013).
20. H. Xu and Y. Shi, "Ultra-compact and broadband silicon polarization rotator," in *Conference on Lasers and Electro-Optics Pacific Rim* (IEEE, 2017), pp. 1–2.
21. H. Xu and Y. Shi, "Ultra-broadband silicon polarization splitter-rotator based on the multi-mode waveguide," Opt. Express **25**, 18485–18491 (2017).
22. H. Wu, Y. Tan, and D. Dai, "Ultra-broadband high-performance polarizing beam splitter on silicon," Opt. Express **25**, 6069–6075 (2017).
23. X. Guan, P. Chen, S. Chen, P. Xu, Y. Shi, and D. Dai, "Low-loss ultra-compact transverse-magnetic-pass polarizer with a silicon subwavelength grating waveguide," Opt. Lett. **39**, 4514–4517 (2014).
24. D. Kim, M. Lee, Y. Kim, and K. Kim, "Ultracompact transverse magnetic mode-pass filter based on one-dimensional photonic crystals with subwavelength structures," Opt. Express **24**, 21560–21565 (2016).
25. B. Bai, X. Li, and Z. Zhou, "Fabrication tolerant TE-pass polarizer based on hybrid plasmonic Bragg grating," in *International Conference on Group IV Photonics* (IEEE, 2016), pp. 132–133.
26. B. Bai, F. Yang, and Z. Zhou, "Demonstration of an on-chip TE-pass polarizer using a silicon hybrid plasmonic grating," Photon. Res. **7**, 289–293 (2019).

27. B. Bai, L. Liu, R. Chen, and Z. Zhou, "Low loss, compact TM-pass polarizer based on hybrid plasmonic grating," IEEE Photon. Technol. Lett. **29**, 607–610 (2017).
28. X. Guan, P. Xu, Y. Shi, and D. Dai, "Ultra-compact and ultra-broadband TE-pass polarizer with a silicon hybrid plasmonic waveguide," Proc. SPIE **8988**, 89880U (2014).
29. H. Xu and Y. Shi, "Flat-top CWDM (de)multiplexer based on MZI with bent directional couplers," IEEE Photon. Technol. Lett. **30**, 169–172 (2017).
30. H. Xu, L. Liu, and Y. Shi, "Polarization-insensitive four-channel coarse wavelength-division (de)multiplexer based on Mach-Zehnder interferometers with bent directional couplers and polarization rotators," Opt. Lett. **43**, 1483–1486 (2018).
31. H. Xu and Y. Shi, "On-chip silicon triplexer based on asymmetrical directional couplers," IEEE Photon. Technol. Lett. **29**, 1265–1268 (2017).
32. D. Liu, M. Zhang, and D. Dai, "Low-loss and low-crosstalk silicon triplexer based on cascaded multimode waveguide gratings," Opt. Lett. **44**, 1304–1307 (2019).
33. J. Chen, Y. Zhang, and Y. Shi, "An on-chip triplexer based on silicon Bragg grating-assisted multimode interference couplers," IEEE Photon. Technol. Lett. **29**, 63–65 (2016).
34. N. Abadía, M. Saber, F. Bello, A. Samani, E. El-Fiky, Y. Wang, J. F. Donegan, and D. V. Plant, "CMOS-compatible multi-band plasmonic TE-pass polarizer," Opt. Express **26**, 30292–30304 (2018).
35. P. J. Bock, P. Cheben, J. H. Schmid, J. Lapointe, A. Delâge, S. Janz, G. C. Aers, D.-X. Xu, A. Densmore, and T. J. Hall, "Subwavelength grating periodic structures in silicon-on-insulator: a new type of microphotonic waveguide," Opt. Express **18**, 20251–20262 (2010).
36. R. Halir, A. Ortega-Moñux, D. Benedikovic, G. Z. Mashanovich, G. J. Wangüemert-Pérez, J. H. Schmid, Í. Molina-Fernández, and P. Cheben, "Subwavelength-grating metamaterial structures for silicon photonic devices," Proc. IEEE **106**, 2144–2157 (2018).
37. P. Cheben, R. Halir, J. H. Schmid, H. A. Atwater, and D. R. Smith, "Subwavelength integrated photonics," Nature **560**, 565–572 (2018).
38. R. Halir, P. J. Bock, P. Cheben, A. Ortega-Moñux, C. Alonso-Ramos, J. H. Schmid, J. Lapointe, D.-X. Xu, J. G. Wangüemert-Pérez, Í. Molina-Fernández, and S. Janz, "Waveguide sub-wavelength structures: a review of principles and applications," Laser Photon. Rev. **9**, 25–49 (2015).
39. P. Cheben, J. H. Schmid, S. Wang, D.-X. Xu, M. Vachon, S. Janz, J. Lapointe, Y. Painchaud, and M.-J. Picard, "Broadband polarization independent nanophotonic coupler for silicon waveguides with ultra-high efficiency," Opt. Express **23**, 22553–22563 (2015).
40. T. Barwicz, A. Janta-Polczynski, M. Khater, Y. Thibodeau, R. Leidy, J. Maling, S. Martel, S. Engelmann, J. S. Orcutt, P. Fortier, and W. M. J. Green, "An O-band metamaterial converter interfacing standard optical fibers to silicon nanophotonic waveguides," in *Optical Fiber Communication Conference*, OSA Technical Digest (online) (Optical Society of America, 2015), paper Th3F.3.
41. D. Benedikovic, P. Cheben, J. H. Schmid, D.-X. Xu, J. Lapointe, S. Wang, R. Halir, A. Ortega-Moñux, S. Janz, and M. Dado, "High-efficiency single etch step apodized surface grating coupler using subwavelength structure," Laser Photon. Rev. **8**, L93–L97 (2014).
42. R. Halir, P. Cheben, J. M. Luque-González, J. D. Sarmiento-Merenguel, J. H. Schmid, G. Wangüemert-Pérez, D.-X. Xu, S. Wang, A. Ortega-Moñux, and Í. Molina-Fernández, "Ultra-broadband nanophotonic beamsplitter using an anisotropic sub-wavelength metamaterial," Laser Photon. Rev. **10**, 1039–1046 (2016).
43. A. Maese-Novo, R. Halir, S. Romero-García, D. Pérez-Galacho, L. Zavargo-Peche, A. Ortega-Moñux, I. Molina-Fernández, J. G. Wangüemert-Pérez, and P. Cheben, "Wavelength independent multimode interference coupler," Opt. Express **21**, 7033–7040 (2013).
44. R. Halir, A. Maese-Novo, A. Ortega-Moñux, I. Molina-Fernández, J. G. Wangüemert-Pérez, P. Cheben, D.-X. Xu, J. H. Schmid, and S. Janz, "Colorless directional coupler with dispersion engineered sub-wavelength structure," Opt. Express **20**, 13470–13477 (2012).
45. H. Xu and Y. Shi, "Ultra-sharp multi-mode waveguide bending assisted with metamaterial-based mode converters," Laser Photon. Rev. **12**, 1700240 (2018).
46. H. Wu, C. Li, L. Song, H.-K. Tsang, J. E. Bowers, and D. Dai, "Ultra-sharp multimode waveguide bends with subwavelength gratings," Laser Photon. Rev. **13**, 1800119 (2019).
47. H. Xu and Y. Shi, "Metamaterial-based Maxwell's fisheye lens for multimode waveguide crossing," Laser Photon. Rev. **12**, 1800094 (2018).
48. H. Wang, Y. Zhang, Y. He, Q. Zhu, L. Sun, and Y. Su, "Compact silicon waveguide mode converter employing dielectric metasurface structure," Adv. Opt. Mater. **7**, 1801191 (2019).
49. H. Xu and Y. Shi, "Ultra-compact polarization-independent directional couplers utilizing a subwavelength structure," Opt. Lett. **42**, 5202–5205 (2017).
50. H. Xu and Y. Shi, "Subwavelength-grating-assisted silicon polarization rotator covering all optical communication bands," Opt. Express **27**, 5588–5597 (2019).
51. H. Xu, D. Dai, and Y. Shi, "Ultra-broadband and ultra-compact on-chip silicon polarization beam splitter by using hetero-anisotropic metamaterials," Laser Photon. Rev. **13**, 1800349 (2019).
52. C. Li and D. Dai, "Compact polarization beam splitter for silicon photonic integrated circuits with a 340-nm-thick silicon core layer," Opt. Lett. **42**, 4243–4246 (2017).
53. Y. Xiong, G. J. Wangüemert-Pérez, D.-X. Xu, J. H. Schmid, P. Cheben, and W. N. Ye, "Polarization splitter and rotator with subwavelength grating for enhanced fabrication tolerance," Opt. Lett. **39**, 6931–6934 (2014).
54. Y. Wang, M. Ma, H. Yun, Z. Lu, X. Wang, N. A. F. Jaeger, and L. Chrostowski, "Ultra-compact sub-wavelength grating polarization splitter-rotator for silicon-on-insulator platform," IEEE Photon. J. **8**, 7805709 (2016).
55. S. Jahani, S. Kim, J. Atkinson, J. C. Wirth, F. Kalhor, A. A. Noman, W. D. Newman, P. Shekhar, K. Han, V. Van, R. G. DeCorby, L. Chrostowski, M. Qi, and Z. Jacob, "Controlling evanescent waves using silicon photonic all-dielectric metamaterials for dense integration," Nat. Commun. **9**, 1893 (2018).
56. Y. Xiong, D.-X. Xu, J. H. Schmid, P. Cheben, and W. N. Ye, "High extinction ratio and broadband silicon TE-pass polarizer using subwavelength grating index engineering," IEEE Photon. J. **7**, 7802107 (2015).
57. C. Gu and P. Yeh, "Form birefringence dispersion in periodic layered media," Opt. Lett. **21**, 504–506 (1996).
58. T. Erdogan, "Cladding-mode resonances in short- and long-period fiber grating filters," J. Opt. Soc. Am. A **14**, 1760–1773 (1997).
59. W. Bogaerts, Y. Xing, and U. Khan, "Layout-aware variability analysis, yield prediction, and optimization in photonic integrated circuits," IEEE J. Sel. Top. Quantum Electron. **25**, 6100413 (2019).
60. D. Taillaert, P. Bienstman, and R. Baets, "Compact efficient broadband grating coupler for silicon-on-insulator waveguides," Opt. Lett. **29**, 2749–2751 (2004).